JOURNAL OF PROPULSION AND POWER
Vol. 22, No. 4, July–August 2006

Numerical Simulation of Injection of Supercritical Ethylene into Nitrogen

Ana M. Star* and Jack R. Edwards†
North Carolina State University, Raleigh, North Carolina
Kuo-Cheng Lin‡ and Susan Cox-Stouffer§
Taitech, Inc., Beavercreek, Ohio 45430
and
Thomas A. Jackson‖
Wright–Patterson Air Force Base, Ohio

DOI: 10.2514/1.16621

A procedure for simulating the injection of supercritical ethylene into nitrogen is used to investigate aspects of the injection of supercritical fuels, considered to be an enabling technology in the design of hydrocarbons-fueled scramjet engines. The method solves the compressible Navier–Stokes equations for an ethylene/nitrogen mixture, with the thermodynamic behavior of ethylene described using the Peng–Robinson equation of state. Homogeneous equilibrium and finite-rate phase-transition models are used to describe the growth of a condensed ethylene phase in several axisymmetric and three-dimensional injector nozzles. Predictions are compared with shadowgraph and direct-lighting imaging data, mass flow rate measurements, mole-fraction and temperature measurements in the jet mixing zone, and wall pressure distributions. Qualitative trends relating to jet structure, the appearance of a condensed phase, and the effects of back pressure and injectant temperature are in good agreement with experimental results but indicate the need for improved characterization of the nozzle flow before injection and the inclusion of a better turbulence model for the jet mixing zone. For conditions where both are applicable, a nucleation/growth phase transition model provides a similar bulk fluid response as a homogeneous equilibrium model but also yields predictions of number density and average droplet size.

Nomenclature

A	=	constant in Peng–Robinson equation
a	=	function in Peng–Robinson equation
B	=	constant in Peng–Robinson equation
b	=	constant in Peng–Robinson equation
C_μ	=	model constant
D	=	diffusion coefficient (m^2/s); also nozzle exit diameter (m)
d	=	droplet diameter (m)
F	=	molecular condensation rate (molecules/s)
f	=	fugacity, Pa
g^*	=	number of molecules in a critical nucleus (molecules/droplet)
h	=	specific enthalpy, J/kg
I	=	nucleation rate [(number of droplets)/(m^3–s)]
k	=	turbulence kinetic energy
k_b	=	Boltzmann's constant
M_w	=	molecular weight (kg/kmol)
m	=	molecular mass (kg)
$\mathcal{N}_A$	=	Avogadro's number
n	=	number density [(number of droplets)/(m^3)])
p	=	pressure, Pa
R	=	universal gas constant [kg/(kmol–K)]
S_c	=	Schmidt number
$S_{c,t}$	=	turbulent Schmidt number
T	=	temperature (K)
t	=	time, s
u_j	=	velocity component in the jth coordinate direction
v	=	molecular volume
X	=	axial direction
x_j	=	jth coordinate direction
Y	=	mass fraction of a phase; also transverse direction
Z	=	compressibility factor; also spanwise direction
α	=	volume fraction
κ	=	function in Peng–Robinson equation
μ	=	molecular viscosity kg/(m–s)
ν	=	kinematic viscosity, m^2/s
ρ	=	density, kg/m^3
$\tilde{\rho}$	=	molar density, $kmol/m^3$
σ	=	interfacial tension (N/m)
τ_K	=	Kolmogorov time scale
ω	=	turbulence frequency, s^{-1}
$\tilde{\omega}$	=	acentric factor

Subscripts

c	=	critical point
chm	=	chamber
coag	=	coagulation
e	=	ethylene
eq	=	equilibrium
I	=	ideal
inj	=	injectant
j	=	index of coordinate direction
l	=	liquid
p	=	derivative with respect to pressure
r	=	reduced property ($Q_r = Q/Q_c$, where Q is a fluid property)

Presented as Paper 4267 at the 33rd AIAA Fluid Dynamics Conference, Orlando, Fl, 21–24 June 2003; received 15 March 2005; revision received 25 January 2006; accepted for publication 25 January 2006.

*Research Assistant, Department of Mechanical and Aerospace Engineering, Campus Box 7910. Student Member AIAA.
†Associate Professor, Department of Mechanical and Aerospace Engineering, Campus Box 7910. Associate Fellow AIAA.
‡Senior Research Scientist, 1430 Oak Court, Suite 301. Senior Member AIAA
§Research Scientist, 1430 Oak Court, Suite 301. Member AIAA.
‖Deputy of Science, AFRL/PRA, 1950 Fifth Street. Senior Member AIAA.

ρ = derivative with respect to density
T = derivative with respect to temperature
v = vapor
vap = vapor
w = wall
Y_v = derivative with respect to vapor-phase mass fraction

Superscripts

l = liquid
v = vapor

Introduction

BECAUSE of the temperature limit of current aerospace materials, U.S. Air Force high-speed propulsion systems cannot be cooled by conventional techniques due to the temperature limit of current aerospace materials. Regenerative fuel cooling of the airframe and the combustor components is an option that has been explored [1]. Endothermic fuels can be used for regenerative cooling, because they act as a heat sink, undergoing endothermic thermal cracking reactions at very high temperatures. These temperatures are usually much higher than the critical temperature of hydrocarbon fuels. The cooling system is thus responsible for the phase transition of endothermic fuels from a liquid phase to a supercritical-fluid phase.

It is important to understand injection processes involving supercritical fuels, because subsequent mixing and chemical reaction will depend on the state of the fuel as it enters the combustor. The injection of fuels at supercritical conditions is thought to be favorable for promoting rapid mixing and ignition, as it should be most similar to gas-phase injection. However, condensation (the formation of liquid-fuel droplets) may occur under certain injection conditions. The potential impact of fuel condensation on scramjet combustion is uncertain, and the factors that underpin condensate growth should be determined in order to predict its occurrence and to enable its control.

In one of the more detailed experimental investigations of supercritical injection processes, Wu et al. [2,3] studied the injection of supercritical ethylene into nitrogen through round-hole (axisymmetric) nozzles. The Wu et al. database considers parametric variations of the injectant temperature, chamber temperature, and chamber pressure and presents a rather complete picture of the effects of these variations on the ethylene jet structure. Shadowgraph imaging of the jet structure indicated the presence of a condensed ethylene liquid phase under certain injection conditions. The onset of this event, presumably driven by homogeneous or heterogeneous nucleation, could not be determined due to difficulties in imaging the internal structure of the round-hole injector used.

Later, Lin et al. [4,5] used a transparent, three-dimensional injector configuration with a square exit cross section to image the onset of condensation. Their work also considered methane/ethylene mixtures as a more realistic surrogate for cracked JP-class fuels, essentially repeating the Wu et al. database in the scope of their data collection [4]. More recently, additional data involving pure ethylene injection through round-hole (axisymmetric) nozzles at lower injectant temperatures has been obtained, as have pressure measurements within some of the transparent, three-dimensional nozzles [5].

In an attempt to explain the occurrence of condensation, Lin et al. [4,5] used perfect-gas Navier–Stokes calculations to provide a baseline flowfield for calculating supersaturation and nucleation rates. Onset locations (as evidenced by a large increase in nucleation rate) were predicted to a reasonable degree, even given inaccuracies in the thermodynamic modeling of the supercritical fluid. However, such an approach cannot account for the effects of condensate growth on the flowfield, nor can it give an indication of the amount of condensate present (in terms of a volume or mass fraction). The present work develops an improved model for the injection process by combining a solution of the Navier–Stokes equations for the supercritical-fluid with two different approaches for condensate growth: one based on a homogeneous equilibrium assumption and the other on classical nucleation/growth theory, as modified for supercritical fluids by Kwauk and Debenedetti [6]. The remainder of this paper describes the computational model and its solution procedure, presents details of experimental measurements conducted in support of this investigation, and concludes with the model's application in simulating the supercritical ethylene injection experiments of Wu et al. [2,3] and Lin et al. [4,5].

Computational Model

Single-Phase State Description

The cases discussed later involve the injection of ethylene, initially at supercritical conditions, into a chamber containing pure gaseous nitrogen. To account for the thermodynamics of the supercritical fluid, it is necessary to use a generalized state equation, defined by the relations $p = p(\rho, T)$ and $h = h(\rho, T)$. In the present work, we use the Peng–Robinson equation of state [7] (EOS), a cubic formulation similar to the van der Waals equation but generally much more accurate in the liquid phase for nonpolar molecules. The Peng–Robinson equation for a single-component fluid is given by

$$p = Z(\tilde{\rho}, T)\tilde{\rho}RT \tag{1}$$

$$Z(\tilde{\rho}, T) = \frac{1}{1 - b\tilde{\rho}} - \frac{a(T)}{RT}\frac{\tilde{\rho}}{[1 + 2b\tilde{\rho} - (b\tilde{\rho})^2]} \tag{2}$$

In this, the function $a(T)$ is defined as

$$a(T) = a(T_c)\alpha(T_r, \tilde{\omega}) \tag{3}$$

with

$$a(T_c) = 0.45724\frac{R^2T_c^2}{p_c} \tag{4}$$

$$\alpha(T_r, \tilde{\omega})^{1/2} = 1 + \kappa(1 - T_r^{1/2}) \tag{5}$$

$$\kappa = 0.37464 + 1.54226\tilde{\omega} - 0.26992\tilde{\omega}^2 \tag{6}$$

$$T_r = T/T_c \tag{7}$$

The constant b is defined as

$$b = 0.07780\frac{RT_c}{p_c} \tag{8}$$

and other functions used in subsequent developments are as follows:

$$A = \frac{a(T)p}{R^2T^2} \tag{9}$$

$$B = \frac{bp}{RT} \tag{10}$$

These parameters are functions of the critical-point temperature T_c and pressure p_c of the fluid and its acentric factor. For ethylene, the following values are used: $T_c = 282.35$ K, $p_c = 5.0418$ MPa, $\tilde{\omega} = 0.077523$. The enthalpy of a real fluid can be written as the sum of an ideal gas enthalpy and a departure function, dependent on the specific form of the equation of state. For the Peng–Robinson EOS,

$$h(\rho, T) = h_I(T) + \frac{1}{M_w}\left[RT(Z - 1) + \frac{T[da(T)/dT] - a(T)}{2\sqrt{2}b} \times \ell_n\left(\frac{Z + (1 + \sqrt{2})B}{Z + (1 - \sqrt{2})B}\right)\right] \tag{11}$$

where $h_I(T)$ is the ideal gas description. Curve fits from McBride et al. [8] are used to define $h_I(T)$.

A typical isotherm ($T < T_c$) for the Peng–Robinson equation is plotted in Fig. 1 on a pressure–density diagram. Clearly indicated is

the vapor regime, where pressure varies nearly linearly with density, and the liquid regime, where large pressure changes are required to induce a density change. For a given pressure and temperature, the solution of Eq. (2) returns one or three values of the compressibility factor Z, the former corresponding to the single-phase region (either liquid or vapor) and the latter corresponding to the two-phase region, where vapor and liquid may coexist. The corresponding densities for a pressure within the two-phase region are shown as points A–C. A and C represent saturated vapor and liquid states, whereas B is physically meaningless. For a particular temperature, the "allowable" two-phase region is bounded by the pressure values at D and E, which are local extrema. The loci of these pressure values for temperatures between the triple and critical points define liquid and vapor spinodal curves, dividing the two-phase region into metastable vapor, unstable, and metastable liquid regions. At a particular pressure between the liquid and vapor spinodal points, the system is in equilibrium, with the vapor and liquid fugacities attaining equal values. This pressure is known as the vapor pressure p_{vap} and is calculated as a function of temperature by iteratively solving the equation

$$f_{v,\text{eq}}(Z_v, T, p_{\text{vap}}) = f_{l,\text{eq}}(Z_l, T, p_{\text{vap}}) \tag{12}$$

where f is given by

$$\ln \frac{f}{p} = Z - 1 - \ln(Z - B) - \frac{A}{2\sqrt{2}B} \ln\left(\frac{Z + (1+\sqrt{2})B}{Z + (1-\sqrt{2})B}\right) \tag{13}$$

The spinodal pressure and density values (points D and E in Fig. 1) can be obtained analytically by solving the quartic equation

$$\left.\frac{\partial p}{\partial \tilde{\rho}}\right|_T = 0$$

discarding two meaningless roots that occur outside the range of validity of the Peng–Robinson equation. The spinodal pressure values bound the actual vapor pressure, and an appropriate linear combination can be used as an initial guess for the iteration described above.

Homogeneous Equilibrium Model

The Peng–Robinson equation (and similar ones) gives no useful information in the unstable parts of the two-phase region. For densities between the spinodal values, it can be shown that the acoustic eigenvalues are complex, meaning that the Euler system is not hyperbolic in time and that conventional time-marching procedures for integrating the equations are ill posed. It is also of note that the liquid spinodal pressure may be negative for high molecular-weight liquids at lower temperatures, implying that the simulated expansion of a liquid might produce reasonable densities, but unphysical pressures, in the metastable region.

One means of avoiding these difficulties starts with the introduction of a void-fraction formalism for the two-phase region and the assumption of thermodynamic and kinematic equilibrium between the phases. For an equilibrium two-phase flow, the vapor pressure $p_{\text{vap}}(T)$ can be obtained from the equation of state as a function of temperature only [Eq. (12)], and the density and temperature are independent variables. Given updated values for the density and temperature at a grid point as determined from a time-integration method, the following procedure is performed:

1) Determine the vapor pressure at that temperature by the by the iterative procedure described above, and compute the saturation densities $\rho_{l,\text{eq}}(T)$ and $\rho_{v,\text{eq}}(T)$ and the saturation enthalpies $h_{l,\text{eq}}(T)$ and $h_{v,\text{eq}}(T)$ using (2) and the enthalpy expression (11)

2) If the density is not between the saturation values or the temperature is greater than the critical value, then the single-phase description given by the Peng–Robinson equation is used to determine the pressure and enthalpy.

3) If the fluid density is within the saturation limits, the equilibrium equation of state for the homogeneous mixture of liquid and vapor is given by

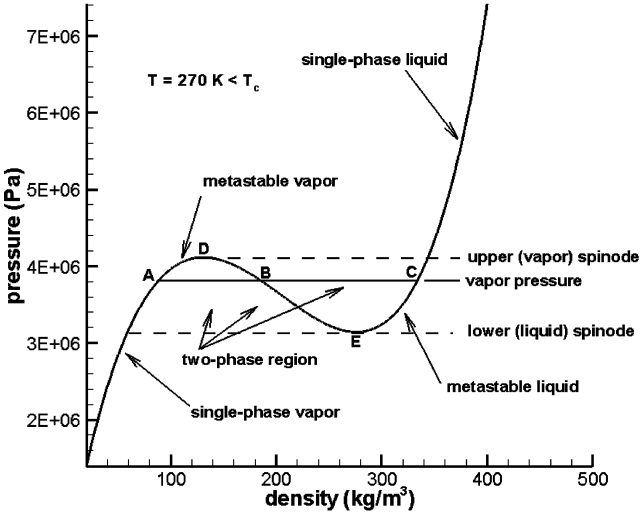

Fig. 1 Pressure–density isotherm: Peng–Robinson equation of state ($T < T_c$).

$$p = p_{\text{vap}}(T) \tag{14}$$

$$\rho h(\rho, T) = \rho_{v,\text{eq}}(T)\alpha_v(\rho, T)h_{v,\text{eq}}(T) + \rho_{l,\text{eq}}(T)\alpha_l(\rho, T)h_{l,\text{eq}}(T) \tag{15}$$

$$\alpha_v(\rho, T) = \frac{\rho - \rho_{l,\text{eq}}(T)}{\rho_{v,\text{eq}}(T) - \rho_{l,\text{eq}}(T)} \tag{16}$$

$$\alpha_l(\rho, T) = 1 - \alpha_v \tag{17}$$

The vapor pressure p_{vap} and the associated saturation-state enthalpies and densities can be calculated directly from the equation of state, thus defining the "vapor dome" in a self-consistent manner.

In this description, the saturation-state values are strict functions of temperature; density dependence is introduced through the void fractions α and latent-heat effects arise through the change in departure enthalpy between the saturation states. The thermodynamic derivatives p_ρ, p_T, $(\rho h)_\rho$, and $(\rho h)_T$ needed in the time-integration method and in the sound speed definition can be computed by straightforward differentiation of the expressions above. The above formulation neglects velocity-slip effects, with the velocity actually solved for being a mass-weighted average velocity, and thermal equilibrium is assumed. This system is hyperbolic in character and is similar to the Euler system in structure but admits such multiphase features as cavitation zones and condensation shocks [9]. A key element is the use of density and temperature as the "working" thermodynamic variables (i.e., the values that the flow solver outputs directly). This choice is driven by the equilibrium closure for the two-phase region, in which pressure and temperature are not independent variables. In the cases presented later, gas-phase mixing rules are used to account for interactions between ethylene and the nitrogen gas in the test chamber. In these, Dalton's law is used to determine a mixture pressure, with the partial pressure of nitrogen gas calculated from the ideal gas equation and that of ethylene calculated using the closure relations above. The mixture enthalpy is determined as a mass-fraction weighted sum of the species enthalpies for ethylene and nitrogen. The nitrogen species enthalpy is obtained from the McBride et al. [8] database. The use of gas-phase mixing rules is believed to be adequate as by the time that the fluids interact, the ethylene has expanded to gaseous densities.

Nucleation/Growth Model

The homogeneous equilibrium model entirely circumvents the possibility of unstable phase transitions but does not allow prediction

of quantities such as droplet (or bubble) number density, nucleation rate, and average droplet (or bubble) size. One approach that can describe nonequilibrium phase transitions is homogeneous nucleation theory, which is strictly valid in the metastable regions of the vapor dome. For a condensation event, the simplest formulation (which outputs an average droplet size, rather than a size distribution, at every mesh point [10]) requires the solution of two additional transport equations, one for the total droplet number density and one for the vapor-phase mass fraction:

$$\frac{\partial n}{\partial t} + \frac{\partial (n u_j)}{\partial x_j} = I + \left.\frac{\partial n}{\partial t}\right|_{\text{coag}} \tag{18}$$

$$\frac{\partial (\rho Y_v)}{\partial t} + \frac{\partial (\rho Y_v u_j)}{\partial x_j} = -\frac{M_w}{\mathcal{N}_A}(g^* I + nF) \tag{19}$$

The nucleation rate I is defined as [6,10]

$$I = \sqrt{\frac{2\sigma}{\pi}}\frac{pM_w}{RT}\frac{\rho_v \alpha_v}{\rho_l m_e^{3/2}}\exp\left[-\frac{16\pi}{3}\frac{\sigma^3 (v_e^l)^2}{k_b T}\left(\frac{1}{\ell_n (f_v/f_{v,\text{eq}})}\right)^2\right] \tag{20}$$

where the ethylene molecular mass m_e is defined as

$$m_e = \frac{M_w}{\mathcal{N}_A} \tag{21}$$

and the liquid ethylene molecular volume as

$$v_e^l = \frac{m_e}{\rho_l} \tag{22}$$

The equilibrium value of the fugacity $f_{v,\text{eq}}$ is determined as a function of the saturation vapor density $\rho_{v,\text{eq}}$ and the temperature through Eq. (13). The interfacial tension σ is curve-fitted as follows [11]:

$$\sigma = \max\left(0.001, 0.001 \times 23.23\frac{T_c - T}{T_c - 133.2}^{11/9}\right) \tag{23}$$

The limiting value of 0.001 is chosen to avoid extremely high nucleation rates near the critical point. In contrast to the homogeneous equilibrium model, the finite-rate formulation requires that the pressure be a working thermodynamic variable, so that liquid and vapor densities ρ_v and ρ_l are determined directly from the solution of the cubic equation of state (given the local pressure and temperature). To account for real-fluid effects, the supersaturation is defined in terms of the ratio of the vapor-phase fugacity f_v to the saturation value $f_{v,\text{eq}}$ rather than the more familiar ratio p/p_{vap}.

The mass transfer source term in Eq. (19) consists of a portion due to the formation of critically sized nuclei and a portion due to molecular condensation onto existing nuclei. In the former, the number of molecules in a critical nucleus is given as [6]

$$g^* = \frac{32\pi}{3}\left(\frac{\sigma (v_e^l)^{2/3}}{k_b T}\right)^3 \left(\frac{1}{(\ell_n\, f_v/f_{v,\text{eq}})}\right)^3 \tag{24}$$

whereas in the latter, the molecular condensation rate is defined as

$$F = 2\pi d D \frac{\alpha_v}{m_e}(\rho_v - \rho_{v,\text{eq}})\frac{1 + K_n}{1 + 1.71K_n + 1.333K_n^2} \tag{25}$$

In this, the Knudsen number is defined as

$$K_n = \frac{2\mu}{\rho_v d}\sqrt{\frac{\pi m_e}{2k_b T}} \tag{26}$$

and the diffusion coefficient D is defined by assuming a constant Schmidt number (0.72):

$$D = \frac{\mu}{S_c \rho_v} \tag{27}$$

The coagulation rate

$$\left.\frac{\partial n}{\partial t}\right|_{\text{coag}}$$

in Eq. (18) may be affected by Brownian motion, mean shear, and Kolmogorov-scale turbulence, among other factors [12]. An examination of the relative effects for a related problem (rapid expansion of supercritical carbon dioxide solutions through similar nozzles) was conducted in Franklin [10], where it was noted that the largest contribution to the coagulation rate is due to Kolmogorov-scale turbulence, which increases the collision frequency of the droplets. As such, only the model of Saffman and Turner [13], as applied to a locally monodisperse collection of droplets, is used in this work:

$$\left.\frac{\partial n}{\partial t}\right|_{\text{turb}} = -\frac{16}{3}\frac{1}{\tau_K}\left(\frac{d}{2}\right)^3 n^2 \tag{28}$$

where the Kolmogorov time scale (for a k–ω model) is

$$\frac{1}{\tau_K} = \sqrt{\frac{C_\mu k\omega}{\nu}} \tag{29}$$

The average droplet diameter d is related to the vapor-phase mass fraction Y_v and the number density n as follows. First, the bulk density of the two-phase mixture is defined using Amagat's law:

$$\frac{1}{\rho} = \frac{Y_v}{\rho_v(p,T)} + \frac{1 - Y_v}{\rho_l(p,T)} \tag{30}$$

Then, the liquid-phase volume fraction α_l is given by the definition

$$\alpha_l = \frac{\rho(1 - Y_v)}{\rho_l(p,T)} \tag{31}$$

and the average droplet diameter is determined by the equivalence

$$\alpha_l = n\frac{\pi}{6}d^3 \tag{32}$$

thus completing the closure. The enthalpy of the two-phase mixture is given by

$$h(p,T,Y_v) = Y_v h_v(p,T) + (1 - Y_v)h_l(p,T) \tag{33}$$

Implementation of the homogeneous nucleation model requires solving for the pressure, vapor-phase mass fraction, and temperature as the working thermodynamic variables. The required thermodynamic derivatives are now ρ_p, ρ_T, ρ_{Y_v}, h_p, h_T, and h_{Y_v}, which again can be obtained from the equation of state and the mixing rules. It should be noted that the present nucleation/growth model, like the homogeneous equilibrium model, assumes kinematic and thermal equilibrium between the phases.

Transport Models

Viscosity and thermal-conductivity expressions for pure-component ethylene and nitrogen are obtained from McBride [8] and Holland [14]. In regions of two-phase flow, the viscosity and thermal conductivity of the ethylene mixture are defined as follows:

$$\mu_e = \alpha_v \mu_{v,e} + \alpha_l \mu_{l,e} \tag{34}$$

$$k_e = \alpha_v k_{v,e} + \alpha_l k_{l,e} \tag{35}$$

In regions where nominally gas-phase ethylene mixes with gaseous nitrogen, Wilke's law is used to provide the mixture viscosity and thermal conductivity. Turbulent effects are modeled using two different approaches. The axisymmetric calculations described later use a one-equation eddy-viscosity transport model due to Menter [15], whereas the three-dimensional calculations use Menter's hybrid k–ϵ/k–ω two-equation model [16]. Turbulent Prandtl and Schmidt numbers are both set to 0.9.

Numerical Methods

Because of the dissimilarity in the working variables needed, calculations were performed using several different in-house computer codes. In all codes, the Favre-averaged compressible Navier–Stokes equations describing a mixture of real fluids are formulated in a generalized coordinate system and are discretized using a finite-volume method. Inviscid fluxes are discretized using LDFSS-2001 [17], a low-diffusion upwinding technique valid for real fluids at all flow speeds. Second-order accuracy is achieved through Van Leer–limited variable extrapolation techniques. Time integration is facilitated through a preconditioning strategy [18], which reconciles the widely varying characteristic speeds present in the system. The first code, used for the axisymmetric simulations, uses an implicit method based on incomplete lower-upper decomposition to advance the solution and incorporates the homogeneous equilibrium model as well as gas-phase mixing rules for ethylene injection into nitrogen. This code has been applied to supercritical-fluids processing of polymeric coatings materials [10] as well as to other applications [9]. The second code solves three-dimensional flows and is a direct extension of the axisymmetric code with the exception of the use of Menter's two-equation turbulence model in place of Menter's one-equation model. This code uses a planar relaxation method to advance the solution and is parallelized using message-passing interface (MPI) for execution on NCSU's Linux Cluster.[¶] The third code, used for the three-dimensional calculations with the nucleation/growth model, is an extension of one previously developed to simulate two-phase water/nitrogen flows within aerated-liquid ("barbotage") fuel injectors [19,20]. A "mixture" model of two-phase flow is incorporated [21], and the Peng–Robinson equation is used to provide both the liquid- and gas-phase state descriptions. This code also uses a planar relaxation method for time integration and is parallelized using MPI.

Geometry and Boundary Conditions

Figure 2 shows a typical grid arrangement used for the axisymmetric calculations in this study. Several different grids with different dimensions were generated to correspond with configurations tested in Wu et al. [2,3] and Lin et al. [4]. The grid shown corresponds to the 1.0 mm nozzle-diameter round-hole injector configuration used in Wu et al. [3] and Lin et al. [4]. The grid is divided into 4 blocks, indicated by the dark lines. Block 1 contains 41×65 mesh points; block 2 contains 65×33 mesh points, block 3 contains 109×65 mesh points, and block 4 contains 109×33 mesh points, giving a total number of interior grid cells of 14976. A finer grid consisting of 4 times as many points in each block was also used for selected calculations. The boundary condition for the inflow boundary of block 1 fixes the total pressure and total enthalpy to their reservoir values and extrapolates the axial velocity from the interior. The outflow boundary condition for blocks 3 and 4 fixes the static pressure to the chamber value and extrapolates the remaining flow variables. A simple extrapolation boundary condition is used for the top of block 4. Part of the inflow boundary of blocks 3 and 4 (extending from the nozzle exit radius to 0.00765 m away from the centerline) is specified as a solid surface corresponding to the end of the actual nozzle apparatus. No-slip, adiabatic wall conditions are enforced on this surface as well as on the upper boundaries of blocks 1 and 2. Symmetry about the centerline is also enforced. A coflow velocity of 10 m/s is specified along the remaining part of the inflow boundary of block 4. This was found to be necessary to ensure a steady-state solution for most conditions. Turbulence inflow parameters correspond to an assumed turbulence intensity of 5%, referenced to an inflow velocity of 2 m/s. The radius of block 1 is used as a characteristic length for completing the specification of the eddy viscosity.

Figure 3 shows X–Y and X–Z views of the 3-D grid used to simulate some of the transparent-injector experiments performed as part of this study. Only the flow in one quarter of the geometry is

[¶]Web address www.ncsu.edu/itd/hpc [cited 28_March_2006].

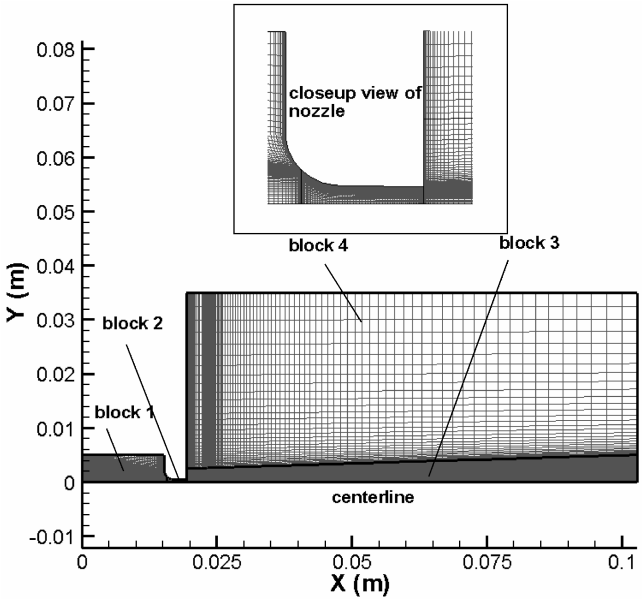

Fig. 2 Grid for axisymmetric nozzle simulations.

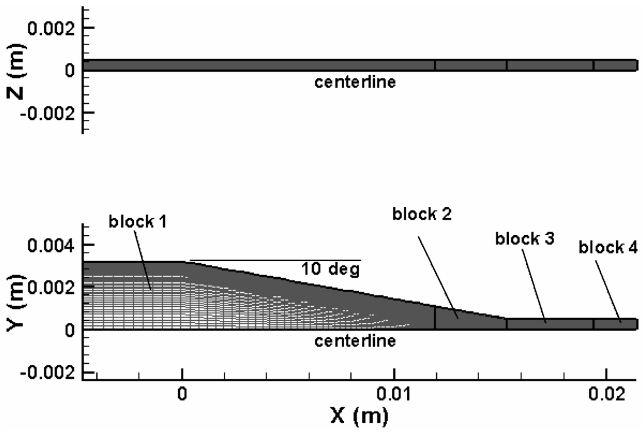

Fig. 3 Grid for three-dimensional nozzle simulations.

actually simulated, as bilateral symmetry is assumed. The exit of the nozzle tube is square in cross section with a width of 1.0 mm, and the entrance angle is 10 deg. A separate grid block was placed outside the domain to allow the expansion of the exiting sonic flow, but no attempt was made to resolve the three-dimensional jet structure external to the nozzle. The $205 \times 65 \times 65$ domain (835,584 interior grid cells) is divided into four blocks. Boundary conditions for the internal flow path are the same as indicated above, except that supersonic outflow conditions are enforced on block 4. Grid-refinement studies were conducted in two dimensions using meshes containing 205×33, 205×65, and 409×129 points.

Experimental Measurements

Pure ethylene was injected vertically downward into a high-pressure chamber filled with room-temperature nitrogen. The apparatus consists of a fuel tank, a heating/chilling unit, a section of heat exchange tube, a solenoid valve, an injector, and the high-pressure chamber, as illustrated in Fig. 4. The test fluid is first prepared inside the fuel tank, which has an internal volume of 15 liters. The test fluid is then introduced into the heat exchange tube to gradually reach the selected temperature. A heating/chilling unit controls the temperature of the ethylene glycol that flows inside the annular passage of the heat exchange tube and is used as the heat exchange medium to control the temperature of the test fluid.

Once the test fluid reaches the desired temperature and pressure, a solenoid valve with a response time of 150 ms is opened for about 5–

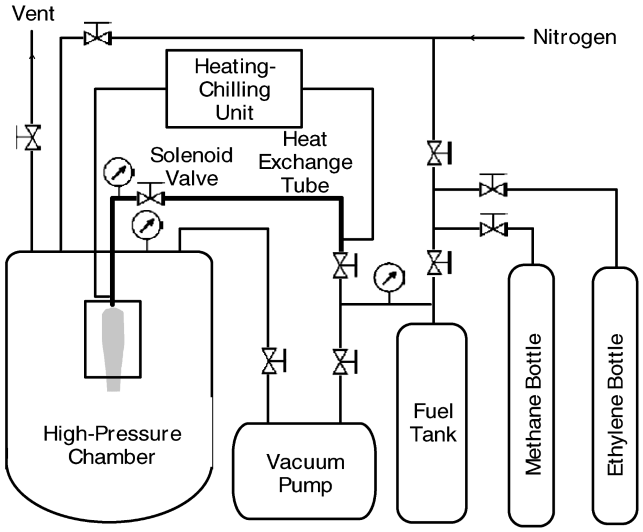

Fig. 4 Schematic of supercritical injection test apparatus.

10 s to charge the test fluid into the test chamber. Because of the transient behavior of the jet, as observed from the time history of a pressure transducer placed just downstream of the solenoid valve, no measurements were made during the first 2 s of injection. After 2 s, the observed pressure transducer reading gradually levels off with a relatively small variation with respect to the injection time. Before injection is begun, the test chamber is flushed with nitrogen twice to remove oxygen and then filled with nitrogen at a desired back pressure for injection. The chamber has an internal diameter of 0.42 m and a height of 0.94 m, resulting in an internal volume of about 0.12 m^3. There are three rectangular quartz windows for optical access and one round port for instrumentation.

A round nozzle with an exit diameter of 1.0 mm was used in the present study. The nozzle passage begins with a 1.6 mm radius entry, which is rounded to avoid flow separation. The entry is followed by a 1 deg converging section to ensure that the choke point can only occur at the nozzle exit. The ratio of passage length to exit diameter was maintained at 4. To study the structure of supercritical fluid inside an injector, a transparent injector with exchangeable internal blocks was also fabricated for the present study. One internal configuration has a 6.4×1.0 mm flow passage, followed by a 10 deg converging section, and then by a 1.0-mm square passage with a length of 4.0 mm. Two quartz windows were fitted into the transparent injector to provide visualization of the fluid structure inside the injector. For the measurement of pressure profiles inside the transparent injector, one quartz block was replaced by a metal block with pressure taps along the injector axis over the desired spatial distribution.

Visualization of the global jet appearance and fluid appearance within the injector was accomplished with shadowgraph and direct-lighting imaging, respectively. Pressure profiles inside the transparent-injector were measured using high-speed pressure transducers. A 45–200 mm zoom lens and a CCD video camera were used to capture the images. The images were either stored inside a computer using a frame grabber or recorded on videotape for later analysis. A Coriolis-type mass flow meter with a measurement range of 2.0–37.8 g/s and an uncertainty of less than 1% was used in the present study to measure the mass flow rate. *K*-type thermocouples were used for temperature measurement in this study. The last thermocouple in the fuel line is located at 99.5 and 88.5 cm from the exits of the transparent and axisymmetric injectors, respectively. This temperature measurement, along with the pressure measurement at approximately the same location, defines the condition of the injectant fluid. The thermocouples were calibrated with an ice bath before each measurement and have an uncertainty of less than ± 0.5 K. Seven pressure transducers were used for pressure measurements inside the high-pressure chamber, fuel tank, and various locations of the fuel line. The pressure profile along the injector axis was measured using a pressure scanner (Scanivalve, Model 3207). All pressure transducers and the pressure scanner were calibrated using a digital pressure gauge (Mensor, Model 2107) and have an uncertainty of less than 0.5%.

Results

Axisymmetric Jet Experiments

The first sequence of test cases focuses on the database of Wu et al. [2,3], which involves injection of pure ethylene through round-hole nozzle configurations with exit diameters of 1.0 and 0.5 mm. This database considers parametric variations of the injectant temperature, chamber temperature, and chamber pressure, and presents a rather complete picture of the effects of these variations on the ethylene jet structure. Not all of these variations are simulated, rather, we focus on conditions that yield the greatest deviations from perfect gas behavior and examine the ability of the hydrodynamic models mentioned above to predict the experimental trends. All of these cases use the homogeneous equilibrium model presented above. Other comparisons with the Wu et al. data may be found in Edwards et al. [22]. Comparisons of results obtained using the Peng–Robinson equation of state with those obtained from an "exact" equation of state for ethylene [23] have been presented in Pinto [24] for some of the cases described in this section. No significant differences were observed.

Figure 5 illustrates the effect of varying the chamber pressure on the jet structure. The reservoir temperature and pressure are set to 293 K and 5.8 MPa, respectively, and the 1 mm nozzle-diameter grid configuration with 14,976 cells is used. To indicate the degree of condensation present and the general flow structure, the images in Fig. 5 plot Mach number line contours superimposed on gray-scale flood contours of liquid-phase volume fraction (ranging between 0 and 0.05) The jets are shown reflected about the centerline for clarity, and the figures are scaled to correspond with shadowgraph images from Wu et al. [2]. For these conditions, the opacity in the shadowgraph images corresponds to the combination of the presence of a condensed phase and general curvature effects in the bulk density field (especially at the higher chamber pressures). Table 1 presents total mass flow rate and condensed liquid mass flow rate as a function of chamber pressure. The method predicts two-phase, choked flow within the injector nozzle, in accord with experimental observations, with only minor deviations observed for the liquid mass flow rate at the highest chamber pressure. For the lowest chamber pressure of 0.14 MPa, the initial rapid expansion of the fluid forces an abrupt shift to mostly gaseous flow. The rapid expansion results in a dome-shaped jet boundary near the nozzle and is terminated by a Mach disk. Experimental results do not indicate the

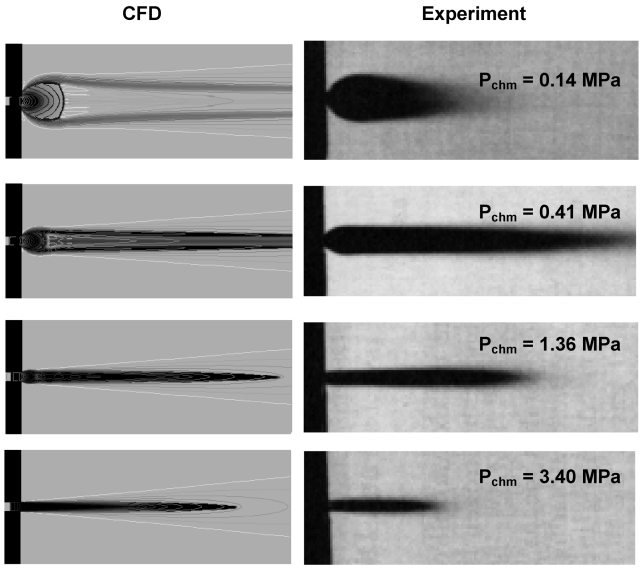

Fig. 5 Effect of chamber pressure on jet structure.

Table 1 Mass flow rates versus chamber pressure (1.0 mm diam nozzle)

Chamber pressure (MPa)	Mass flow rate (g/s)	Liquid mass flow rate (g/s)
3.4	12.91	2.239
1.36	13.02	2.379
0.41	13.05	2.353
0.14	13.03	2.334

presence of the Mach disk due to the masking effects of fuel condensation. At this condition, the liquid content in the core of the jet is greatly reduced downstream of the Mach disk. This provides one explanation of the "feathered" appearance of the jet in Fig. 5. A weaker Mach disk is present for a chamber pressure of 0.41 MPa, whereas for a chamber pressure of 1.36 MPa, the Mach disk is replaced by a sequence of expansion fan/oblique shock-wave interactions. At the highest chamber pressure of 3.4 MPa, the nozzle flow is still choked by virtue of the lower sound speed of the two-phase mixture but the flow expands very little external to the nozzle. The volume fraction of ethylene liquid in the jet increases with the increase in chamber pressure but is nowhere larger than 5%. It appears that the extent of condensed-phase penetration is generally larger in the calculations than indicated in the experimental data. This could be a consequence of the homogeneous equilibrium assumption, but turbulent dispersal of the droplets in the experiment could also explain some of the differences. Otherwise, the predicted jet structure for each case (quantified by the jet spreading rate, presence/absence of a Mach disk, and amount of liquid content) is in good qualitative agreement with the shadowgraph images.

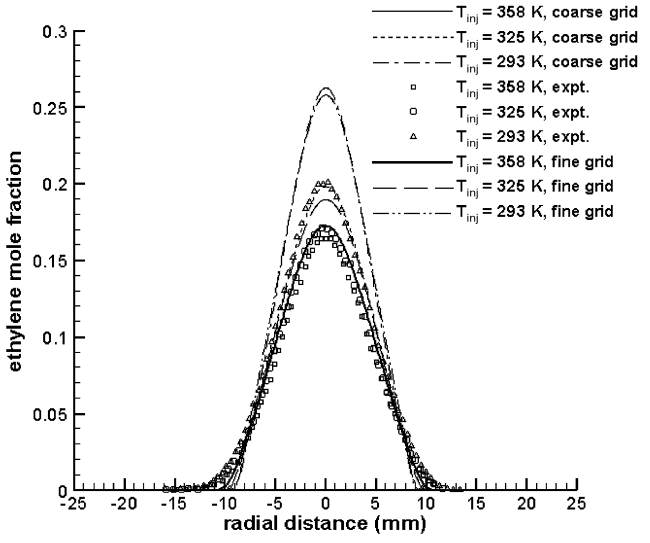

Fig. 6 Ethylene mole fraction distributions at $X/D = 112$.

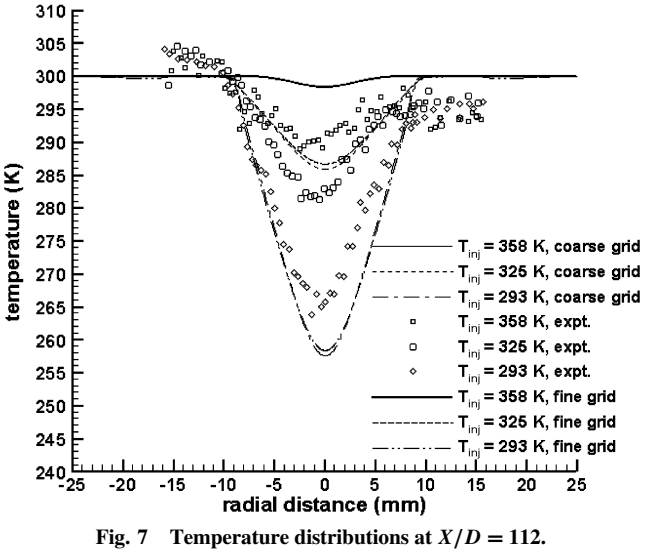

Fig. 7 Temperature distributions at $X/D = 112$.

Figures 6 and 7 correspond to the 0.5 mm nozzle exit diameter geometry, for which radial ethylene mole fraction and temperature profiles at $X/D = 112$ have been obtained for a selection of injectant temperatures [3]. These cases serve to test the ability of the numerical schemes to predict the far-field mixing of the ethylene jet with entrained nitrogen and as such, are as much of a test of the turbulence model as a test of the thermodynamic state description. Radial profiles of ethylene mole fraction are presented in Fig. 6. The lateral spreading of the jet at this location is reasonably well predicted, but the peak (centerline) values of the mole fraction at the lower temperatures are larger than the measured values. Only at the highest injectant temperature of 358 K (a nearly gas-phase expansion) are the predictions in good accord with the experimental data. The results at lower injectant temperatures seem to imply insufficient mixing of the higher-momentum ethylene jet with the surrounding nitrogen gas. A fourfold doubling of the mesh points within the domain (from 14,976 to 59,904 interior cells) provides some slight improvements at the lowest temperature of 293 K but does not significantly affect predictions at the higher temperatures. In contrast, radial temperature profiles shown in Fig. 7 indicate reasonably good agreement with experimental data at injectant temperatures of 293 and 325 K. The experimental results are not symmetric, indicating either a geometry misalignment or laser-beam extinction [3]. This makes the results somewhat difficult to interpret, as there is a 10 deg difference between the measured far-field values on either side of the jet (the calculation assumes a chamber temperature of 300 K). The calculations underpredict the measured temperature deficit at the centerline for the highest temperature, and again, the effects of grid refinement are minimal. The use of a 10 m/s coflow to model nitrogen entrainment probably affects these results to some degree. Lower values for the coflow velocity led to an unacceptable level of unsteadiness in the jet shear layer, particularly on the fine grid.

In a more recent effort, Lin et al. [4,5] have repeated many of the axisymmetric-jet experiments of Wu et al. [2,3], focusing primarily on the structure of methane/ethylene jets. Predictions using a simplified treatment of methane/ethylene mixtures within the framework of the homogeneous equilibrium model have been presented in Lindau et al. [22]. Several imaging studies have also been performed for pure ethylene jets, emphazing the effects of injectant temperatures nearer the critical point on the jet structure [5]. These are used in the present study. Figure 8 compares predictions of the jet structure with shadowgraph images for a selection of injectant temperatures. The injectant pressure varies from 6.19 to 6.25 MPa, and the fine grid with 55,904 interior cells was used in these calculations. The injectant pressure is above the critical pressure of 5.018 MPa and the injectant temperatures range from 280.6 K ($0.994T_c$) to 311.6 K ($1.103T_c$). As in Fig. 5, a combination of line contours of Mach number and gray-scale flood contours of liquid ethylene volume fraction is used to provide indications of the Mach-disk structure, the jet spreading rate, and the amount of condensation present. The volume-fraction contour levels range from 0 to 0.005, and the same scale is used for all figures. The Mach-number contour levels are adjusted for each figure. Good visual agreement in the positioning of the Mach disk, the initial spreading rate of the jet, and the narrowing of the condensation plume downstream of the Mach disk is indicated for the higher temperatures of 311.3 and 300.1 K. At the highest temperature of 311.3 K, there is little experimental evidence of the condensed phase persisting beyond the nozzle exit, though some liquid is predicted to be entrained into the shear layer and carried around the Mach disk. As the temperature is lowered, the amount of condensation present increases, leading to the complete masking of the internal jet structure at $T = 294.8$ deg. The predictions show that even at this temperature, the amount of liquid material that is maintained as the flow passes through the Mach disk is relatively small, compared with the amount exiting the nozzle. The initial spreading angle is visually similar to that in the experiment,

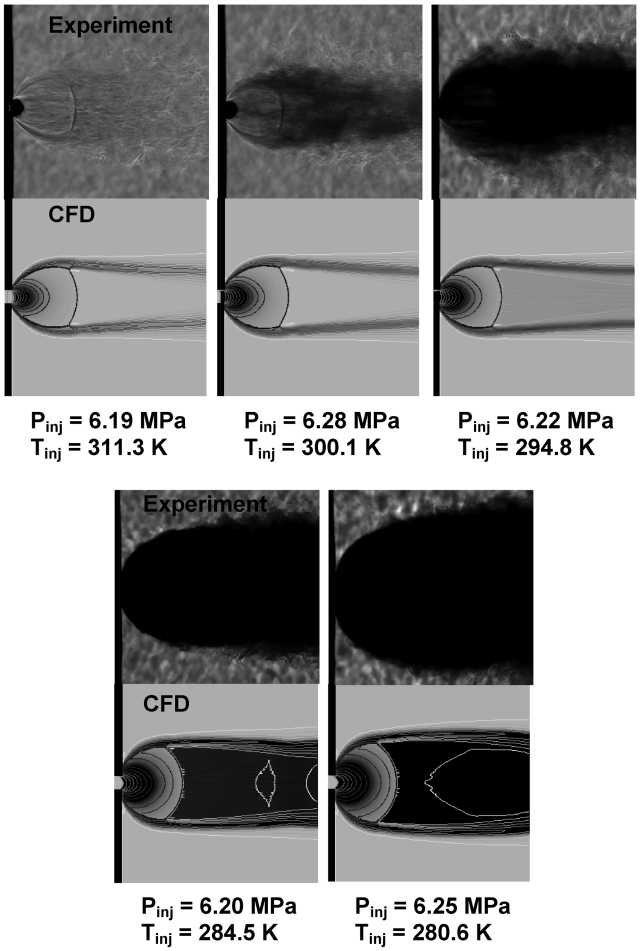

Fig. 8 Effect of injectant temperature on jet structure.

though the amount of liquid-droplet entrainment into the outer edges of the shear layer appears to be underpredicted. The trend of increasing amounts of liquid in the jet with decreasing injectant temperatures is maintained for the lower injectant temperatures of 284.5 K and 280.6 K. The predicted liquid-phase volume fraction at the nozzle exit is around 14% for the lowest temperature of 280.6 K, implying that the potential for forming larger droplets that do not immediately vaporize is high. Again, the initial spreading rate appears to be captured reasonably well, but the calculated extent of condensed-phase penetration towards the outer parts of the shear layer is underpredicted. This effect is particularly noticeable for the lowest temperature, where the calculation predicts a jet that is much less broad in the radial direction than is indicated in the image. As the actual Mach-disk structure cannot be seen at this temperature, it is uncertain whether the broadening effect is due to a much larger Mach disk or simply to the entrainment of droplets into the shear layer that separates the free-jet expansion zone from the quiescent gas. The equilibrium assumptions would appear to break down in this region. Similar to the observations in Wu et al. [2,3] and Lin et al. [4], the position of the Mach disk along the centerline is observed to be relatively independent of the injectant temperature; however, the diameter of the Mach disk increases with decreasing injectant temperature.

Table 2 presents mass flow rate predictions versus experimental data. Deviations become more significant at the lower temperatures, which are nearer the critical point. The underprediction of the mass flow rate at the lowest temperature of 280.6 K, as well as the underprediction of the broadening of the jet in Fig. 8, would indicate that the actual density of the fluid upstream of the nozzle entrance region is higher than predicted by the Peng–Robinson equation of state. This could imply that the temperature just upstream of the entrance to the nozzle is actually lower than the measured value of 280.6. Doubling the number of mesh points slightly improves agreement with the measured values.

Ethylene Injection Experiments (Transparent-Injector Geometry)

Lin et al. [4,5] report initial results for supercritical methane/ethylene jet expansion from a selection of three-dimensional, transparent-injector configurations. The use of nominally rectangular, rather than circular, injector cross sections allows for shadowgraph imaging of the onset of condensation within the nozzle. The transparent injector considered in this work consists of a 10 deg contraction followed by a 4 mm straight nozzle with a 1 mm square exit cross section. Figure 9 compares direct-lighting imaging data for pure-ethylene injection with liquid-phase void-fraction predictions for injectant temperatures of 309.2, 289.0, 283.9, and 281.5 K and a nominal injectant pressure of around 5.45 MPa. The homogeneous equilibrium model is used in these calculations. Darker contours indicate the formation of a condensed phase at the entrance to the straight nozzle section for injectant temperatures of 289.0, 283.9, and 281.5 K. At the injectant temperature of 309.2 K, a condensed phase is not formed within the nozzle, but some condensation is evident in the predictions of the flow within the simulated expansion region external to the nozzle. This is in good agreement with imaging results. The relative amount of condensation is indicated by an increase in gray-scale contrast, and again, good visual agreement with the direct-lighting images is indicated.

Further insights into the formation of a condensed phase within the nozzle can be found by plotting pressure versus mixture density (along the centerline) for the different injectant temperatures (Fig. 10). These plots are indicative of the equilibrium thermodynamic process path followed during a nearly isentropic expansion of the fluid from the nozzle reservoir conditions to the free-jet expansion zone. The vapor dome and spinodal curves provided by the Peng–Robinson equation of state are also shown in Fig. 10. From the figure, one can see that the saturated-vapor line is crossed for injectant temperatures of 309.2 and 289.9 K, whereas the saturated liquid line is crossed for injectant temperatures of 283.9 and 281.5 K. For the higher temperatures, the process path for the two-phase mixture is contained within the metastable vapor region, implying that the phase transition involves the formation of a dispersed liquid phase from a supersaturated vapor. As the process path does not cross the vapor spinodal curve, it is probable that homogenous nucleation theory could be used to model this phase transition as a relaxation process through a sequence of metastable states. The situation is different for injectant temperatures of 283.9 and 281.5 K. Here, the process path enters the metastable liquid region then progresses into the unstable region, where the equation of state (under nonequilibrium conditions) would not be expected to apply. This process could be viewed as the formation of a dispersed vapor (bubble) phase from a supersaturated liquid and could be regarded as a cavitation event rather than a condensation event. Homogeneous nucleation theory could be used to describe the initial

Table 2 Predicted and measured mass flow rates versus injectant temperature

P_{inj} (MPa)	T_{inj} (K)	Mass flow rate (g/s) (experiment)	Mass flow (g/s) (coarse grid)	Mass flow rate (g/s) (fine grid)
6.19	311.3	13.10	13.04	13.23
6.28	300.1	15.31	14.56	14.76
6.22	294.8	17.88	15.29	15.47
6.20	284.5	23.33	21.80	22.20
6.25	280.6	30.28	25.38	25.86

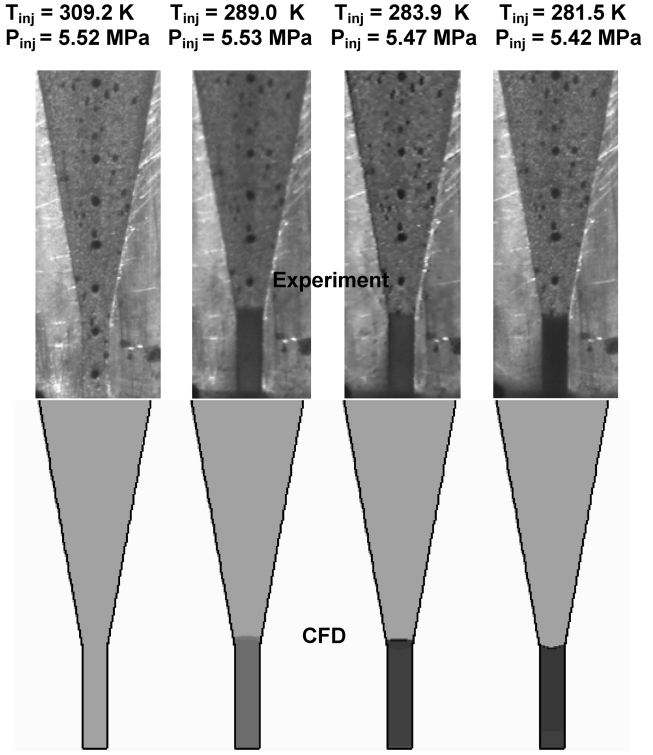

Fig. 9 Effect of injectant temperature on onset of condensation in transparent injector.

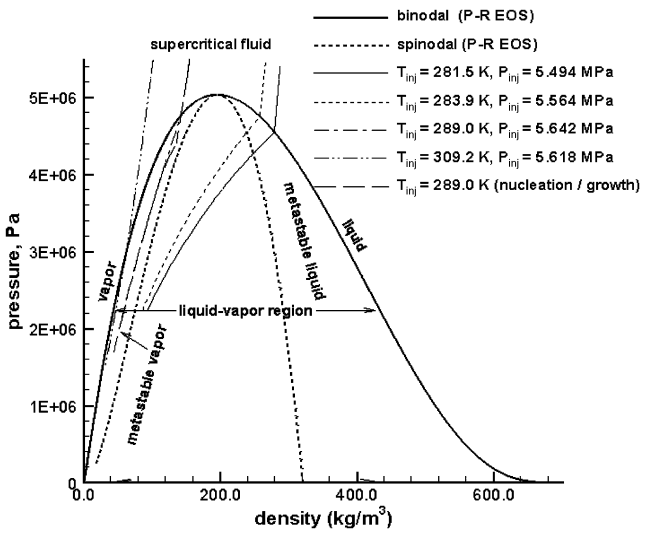

Fig. 10 Centerline pressure–density process paths for different injectant temperatures.

stages of the phase transition that occur within the metastable liquid region, but if the rate of vapor mass generation is not fast enough to force the local pressure to equilibrate rapidly to the vapor pressure (Fig. 1), the process path could cross the liquid spinodal curve. When this happens, the solution of the cubic equation of state would result in one vapor density, rather than three. This implies the spontaneous, irreversible formation of a vapor phase, which would act rapidly to break up the liquid media into filaments and droplets. The rate process associated with this transition is not described by homogeneous nucleation theory. The equilibrium approach used in these calculations implies an infinitely fast phase-transition rate and avoids this difficulty entirely. Details of the transition process itself, such as local droplet size and population, cannot be determined, however.

Figure 11 illustrates the effect of mesh refinement on two-dimensional predictions of the centerline pressure within the injector

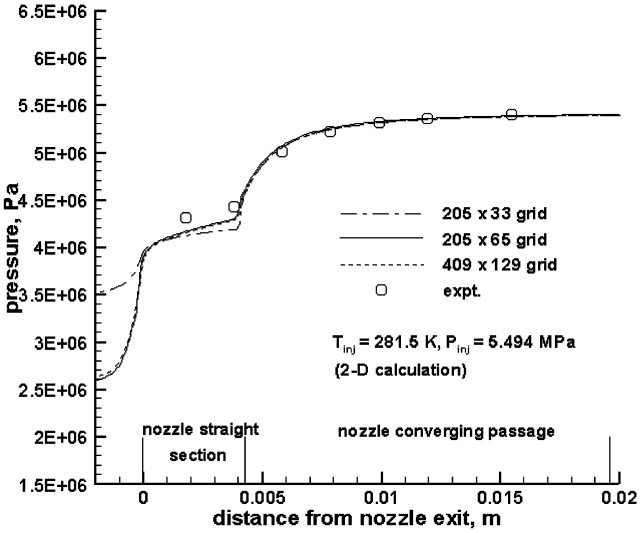

Fig. 11 Effect of mesh refinement on wall pressure distributions at $T_{inj} = 281.5$ K (two-dimensional calculations); nozzle exit at $X = 0$; flow from right to left.

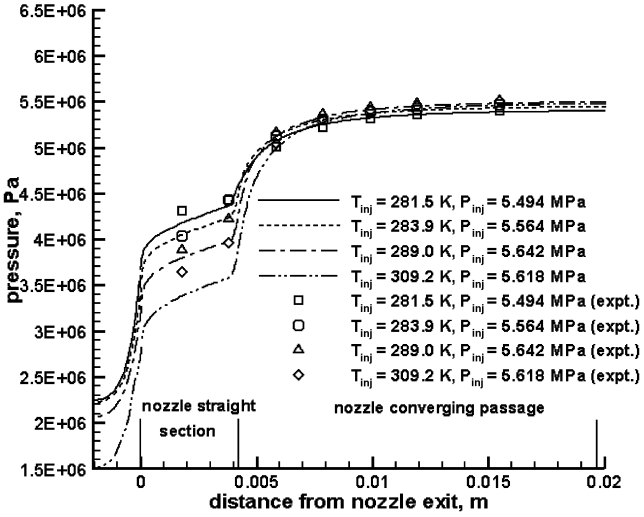

Fig. 12 Effect of injectant temperature on wall pressure distributions; nozzle exit at $X = 0$; flow from right to left.

for an injectant temperature of 281.5 K. A two-dimensional mesh-refinement study was conducted to reduce computational expense; the validity of this assumption may be assessed by comparing Figs. 11 and 12, which presents three-dimensional predictions on the $205 \times 65 \times 65$ mesh. The pressure distributions corresponding to the 205×65 and 405×65 meshes are virtually identical. Figure 12 compares pressure distributions at all injectant temperatures with experimental data. Generally good agreement is observed, except for the highest temperature of 309.2 K. As this is the case that should be influenced the least by real-fluid effects, the discrepancy is somewhat surprising and is as yet unexplained. The general trend with decreasing injectant temperature is to reduce the amount of expansion that occurs within the nozzle itself. This is consistent with the presence of more liquid content with decreasing injectant temperature, as evidenced in Fig. 13, a plot of centerline ethylene liquid volume fraction versus distance away from the nozzle exit. Reflecting observations noted above, the reservoir liquid volume fraction is set to one for the two lowest temperatures and zero for the two highest temperatures. The appearance of a liquid phase at the highest temperature of 309.2 K is confined to the external expansion region, whereas in the other cases, the phase transition is initiated at the entrance to the straight nozzle section. The decrease in liquid content as the flow proceeds toward the nozzle exit is significant at

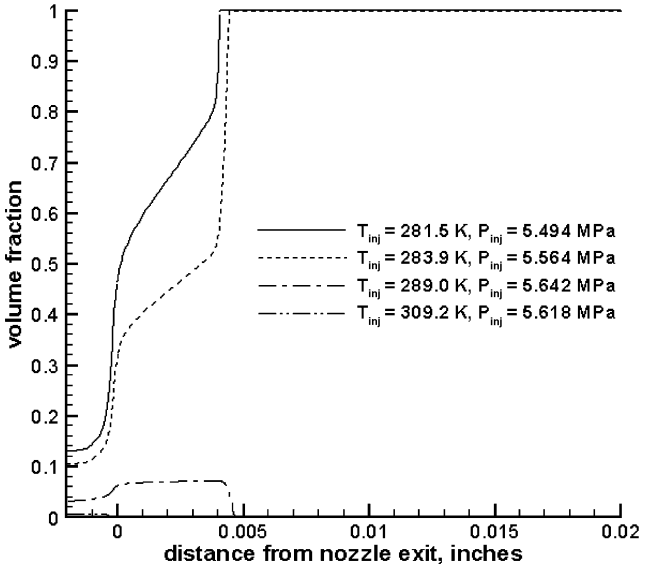

Fig. 13 Effect of injectant temperature on centerline liquid volume fraction; nozzle exit at $X = 0$; flow from right to left.

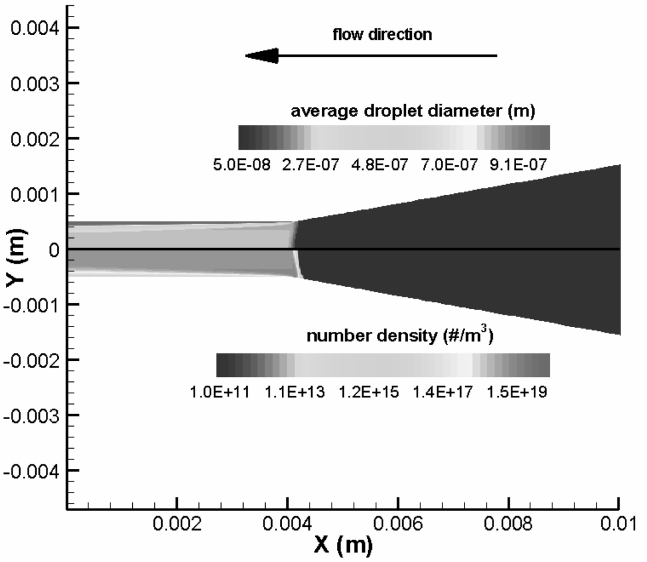

Fig. 15 Contour plots of average droplet diameter (top) and droplet number density (bottom); nozzle exit at $X = 0$; flow from right to left.

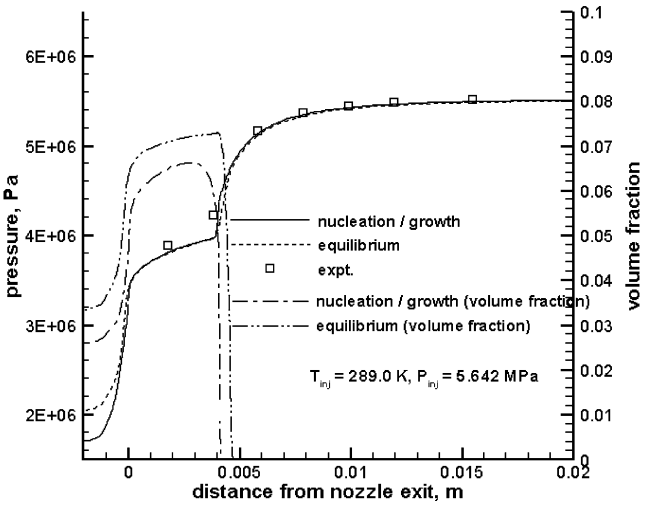

Fig. 14 Pressure and liquid volume-fraction distributions at $T_{inj} = 289.0$ K: homogeneous equilibrium model and nucleation/growth model; nozzle exit at $X = 0$; flow from right to left.

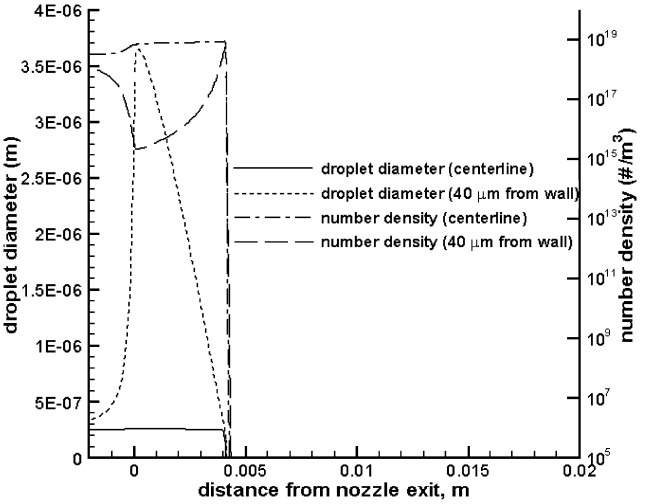

Fig. 16 Average droplet diameter and number density distributions (centerline and near wall); nozzle exit at $X = 0$; flow from right to left.

the lowest two temperatures, whereas the liquid content stays more constant within the nozzle for the 289.0 K case.

Figures 14–16 present results from the nucleation/growth model as applied to the 289.0 K case. Figure 14 compares centerline pressure and volume-fraction distributions as obtained from the homogeneous equilibrium model and the nucleation/growth model. Pressure distributions are virtually identical except near the condensation onset region, where the nucleation/growth model results in slightly higher pressures and slightly better agreement with the experimental data. The pressure–density process path for the nucleation/growth model is also shown in Fig. 10, where it can be seen that it follows the equilibrium distribution for much of the expansion but ventures nearer to the spinodal curve after crossing the saturated-vapor curve. Figure 14 also shows that the rate of formation of the liquid phase (in terms of its volume fraction) is less than predicted by the equilibrium model and that the overall amount of liquid produced within the nozzle is also less. Both of these trends are as expected. Figure 15 provides contour plots of average droplet diameter and number density within the nozzle. Though the volume and mass-fraction distributions (not shown) are nearly homogeneous in the Y direction, the number-density and droplet-diameter distributions vary significantly near the wall. Figure 16 provides more detail, showing distributions obtained along the centerline and within the sidewall boundary layer. Near the wall, high strain rates result in a decrease in the modeled Kolmogorov time scale [Eq. (29)], effectively increasing the droplet coagulation rate. This results in a reduction in the droplet number density in this region, and as the volume fraction is nearly constant, the average droplet diameter increases through Eq. (32). Super-micron-sized (3.5 μm) droplets are eventually formed within the boundary layer, whereas submicron sized (0.3 μm) droplets are formed nearer the centerline. Such large droplets would tend to maintain their initial momentum and would vaporize more slowly upon exiting the nozzle, compared with the smaller droplets formed within the core fluid. This would provide one explanation for the apparent presence of a significant amount of liquid content in the outer edges of the shear layer (Fig. 5), which is not found in the equilibrium predictions. It is straightforward to modify the nucleation/growth model to account for bubble formation within a supersaturated liquid. This was done, and attempts were made to simulate the nozzle flowfields for the 283.9 and 281.5 K injectant temperatures. In these cases, the nucleation rate was not fast enough to induce a rapid relaxation to the equilibrium condition, and the calculations eventually diverged due to the instantaneous appearance of vapor regions. It is possible that the use of more ad hoc

return-to-equilibrium rate expressions [21], if calibrated properly, could prevent this response.

Conclusions

A computational fluid dynamics approach for the simulating the expansion of supercritical ethylene within axisymmetric and three-dimensional nozzle configurations has been applied to geometries and test conditions used by Wu et al. [2,3] and Lin et al. [4,5] in their experimental investigations. Two approaches for modeling condensate growth, a homogeneous equilibrium model and a finite-rate nucleation/growth model, have been implemented and tested. Many of the qualitative observations made in the experiments have been confirmed in the simulations, including

1) decreased amounts of condensate in the ethylene jets with increasing injectant temperature,

2) increased amounts of condensate in the ethylene jets with increasing chamber pressure,

3) establishment of a choked-flow state at low injectant temperatures, even for high chamber pressures,

4) sensitivity of the position of the Mach disk with changing injectant temperature,

5) decreasing expansion angle of the exiting jet with increasing injectant temperature.

In addition, predictions of the onset of the phase transition within the nozzles are in good agreement with direct-lighting imaging results. Predictions of the pressure distributions within the injectors and mass flow rates are also in good agreement with measured data. Direct comparisons of the extent of condensate penetration into the jet mixing zone indicate that the homogeneous equilibrium model (which also implies kinematic and thermal phase equilibrium) may be inadequate in this region, due to the presence of large droplets that do not vaporize rapidly and may not follow the flow. Quantitative predictions of mole fraction profiles and temperature profiles exhibit some deviations from the experimental measurements, indicating that further improvements in the characterization of the nozzle flow before injection and in modeling turbulence effects in the jet mixing zone are necessary.

Where both are applicable, the nucleation/growth model provides predictions similar to that of the homogeneous equilibrium model but also yields three-dimensional droplet-diameter and number-density distributions. The use of this model appears to be restricted to higher injectant temperatures, where the formation of a disperse liquid-phase from a supersaturated vapor is the expected physical response.

Acknowledgements

This research was supported by Taitech, Inc., under a subcontract from Taitech's base contract F33615-02-C-2234 with the U.S. Air Force. Computer time was provided by the High Performance Computing component of North Carolina State University's Information Technologies Division (www.ncsu.edu/itd/hpc [cited 28 March 2006]).

References

[1] Edwards, T., "USAF Supercritical Hydrocarbon Fuels Interests," AIAA Paper 93-0807, Jan. 1993.

[2] Wu, P.-K., Chen, T. H., Nejad, A. S., and Carter, C. D., "Injection of Supercritical Ethylene into Nitrogen," *Journal of Propulsion and Power*, Vol. 12, No. 4, 1996, pp. 770–777.

[3] Wu, P.-K., Shahnam, M., Kirkendall, K. A., Carter, C. D., and Nejad, A. S., "Expansion and Mixing Processes of Underexpanded Supercritical Fuel Jets Injected into Superheated Conditions," *Journal of Propulsion and Power*, Vol. 15, No. 5, 1999, pp. 642–649.

[4] Lin, K.-C., Cox-Stouffer, S., Kennedy, P. J., and Jackson, T. A., "Expansion of Supercritical Methane/Ethylene Jets in a Quiescent Subcritical Environment," AIAA Paper 2003-0483, Jan. 2003.

[5] Lin, K.-C., Cox-Stouffer, S., and Jackson, T. A., "Structures and Phase Transition Processes of Supercritical Methane/Ethylene Mixtures Injected into a Subcritical Environment," *Combustion Science and Technology*, Vol. 178, Nos. 1–3, 2006, pp. 129–160.

[6] Kwauk, X., and Debenedetti, P. G., "Mathematical Modelling of Aerosol Formation by Rapid Expansion of Supercritical Solutions in a Converging Nozzle," *Journal of Aerosol Science*, Vol. 24, No. 4, 1993, pp. 445–469.

[7] Peng, D.-Y., and Robinson, D. B., "A New Two-Constant Equation of State," *Industrial and Engineering Chemistry Fundamentals*, Vol. 15, No. 1, 1976, pp. 59–64.

[8] McBride, B. J., Gordon, S., and Reno, M. A., "Coefficients for Calculating Thermodynamic and Transport Properties of Individual Species," NASA TM-4513, Oct. 1993.

[9] Edwards, J. R., Franklin, R. K., and Liou, M.-S., "Low Diffusion Flux-Splitting Methods for Real Fluid Flows with Phase Transitions," *AIAA Journal*, Vol. 38, No. 9, 2000, pp. 1624–1634.

[10] Franklin, R. K., Edwards, J. R., Chernyak, Y., Gould, R. D., Henon, F., and Carbonell, R. G., "Formation of Perfluoropolyether Coatings by the Rapid Expansion of Supercritical Solutions (RESS) Process. Part 2: Numerical Modeling," *Industrial and Engineering Chemistry Research*, Vol. 40, No. 23, 2001, pp. 6127–6139.

[11] Lide, D. (ed.), *Handbook of Chemistry and Physics*, 85th ed., Taylor and Francis, Boca Raton, Florida, 2005.

[12] Friedlander, S. K., *Smoke, Dust, and Haze: Fundamentals of Aerosol Behavior*, Wiley Interscience, New York, 1977.

[13] Saffman, P., and Turner, J., "On the Collision of Drops in Turbulent Clouds," *Journal of Fluid Mechanics* Vol. 1, No. 1, 1956, p. 16.

[14] Holland, P. M., Eaton, B. E., and Hanley, H. J. M., "A Correlation of the Viscosity and Thermal Conductivity Data of Gaseous and Liquid Ethylene," *Journal of Physical and Chemical Reference Data*, Vol. 12, No. 3, 1983, pp. 917–932.

[15] Menter, F. R., "Eddy Viscosity Transport Equations and Their Relation to the *k*–Epsilon Model," *Journal of Fluids Engineering*, Vol. 119, No. 12, 1997, pp. 876–884.

[16] Menter, F. R., "Two Equation Eddy Viscosity Turbulence Models for Engineering Applications," *AIAA Journal*, Vol. 32, No. 8, 1994, pp. 1598–1605.

[17] Edwards, J. R., "Towards Unified CFD Simulations of Real Fluid Flows," AIAA Paper 2001-2524CP, June 2001.

[18] Weiss, J. M., and Smith, W. A., "Preconditioning Applied to Variable and Constant Density Flows," *AIAA Journal*, Vol. 33, No. 11, 1995, pp. 2050–2057.

[19] Tian, M., Edwards, J. R., Lin, K.-C., and Jackson, T. A., "Numerical Simulation of Transient Two-Phase Flow Within Aerated-Liquid Injectors," AIAA Paper 2003-4226, June 2003.

[20] Tian, M., Xiao, X., Edwards, J. R., Lin, K.-C., and Jackson, T. A., "Numerical Simulation and Experimental Characterization of the Internal Two-Phase Flow Within an Aerated Liquid Injector," AIAA Paper 2004-2645, June 2004.

[21] Lindau, J. W., Venkateswaran, S., Kunz, R. F., and Merkle, C. W., "Development of a Fully Compressible Multi-Phase Reynolds-Averaged Navier–Stokes Model," AIAA Paper 2001-2648, June 2001.

[22] Edwards, J. R., Pinto, A. M., Lin, K.-C., and Jackson, T. A., "Simulation of Injection of Supercritical Methane/Ethylene Mixtures into Nitrogen," AIAA Paper 2003-4267, June 2003.

[23] Smukula, J., Span, R., and Wagner, W., "New Equation of State for Ethylene Covering the Fluid Region for Temperatures from the Melting Line to 450 K at Pressures up to 300 MPa," *Journal of Physical and Chemical Reference Data*, Vol. 29, No. 5, 2000, pp. 1053–1119.

[24] Pinto, A. M., "Two-Dimensional Simulation of Injection of Supercritical Ethylene in Nitrogen," *Region 5 AIAA Student Conference Paper*, AIAA Paper No. RSC2-2003-U-023, April 2003.

J. Oefelein
Associate Editor